ADVANCED FUNCTIONAL MATERIALS
www.afm-journal.de

Epitaxial Interface-Driven Photoresponse Enhancement in Monolayer WS_2–MoS_2 Lateral Heterostructures

Pargam Vashishtha, Clara Kofler, Ajay Kumar Verma, Sindhu Priya Giridhar, Jonathan O. Tollerud, Nethmi S. L. Dissanayake, Tanish Gupta, Manoj Sehrawat, Vishnu Aggarwal, Edwin L.H. Mayes, Billy J. Murdoch, Deepak Sharma, Taimur Ahmed, Jani Kotakoski, Jeffrey A. Davis, Yuerui Lu, Govind Gupta, Irfan H. Abidi, and Sumeet Walia**

2D transition metal dichalcogenides heterostructures are driving advancements in next-generation optoelectronic technologies. Lateral 2D heterojunctions with atomically seamless interfaces play a vital role in modulating charge separation and carrier dynamics, yet underlying transport mechanisms remain inadequately understood, limiting practical deployment. Here, monolayer WS_2-MoS_2 lateral edge-epitaxial heterostructures synthesized via chemical vapor deposition (CVD), providing critical insights into heterointerface effects on charge distribution and photoresponse are reported. Photodetector fabricated from this heterostructures exhibit broadband spectral response from ultraviolet to near-infrared, achieving peak responsivity of 1850 mA W^{-1} and detectivity of 4.36×10^{11} Jones under 565 nm illumination. This represents ≈200% enhancement compared to individual monolayer MoS_2 or WS_2 devices, directly demonstrating the synergistic benefits of lateral heterostructure engineering. Spatially resolved surface potential mapping and second-harmonic generation imaging reveal that enhanced performance originates at the epitaxial interface, confirming the critical role of interfacial electric fields and nonlinear optical effects in charge carrier dynamics. The characterization provides direct experimental evidence linking atomically seamless interface properties to macroscopic device performance enhancements. These findings underscore the significant potential of CVD-grown WS_2-MoS_2 lateral heterostructures for high-performance photodetectors and establish interface engineering as a powerful strategy for advancing 2D semiconductor device technologies.

1. Introduction

2D materials, particularly transition metal dichalcogenides (TMDs), have garnered significant attention as promising candidates for semiconducting materials in the development of miniaturized, energy-efficient electronic and optoelectronic devices.[1–5] They offer distinct advantages, including environmental stability, a direct bandgap in their monolayer form, and thickness-dependent tunable electronic and optical properties.[6] These attributes make TMDs ideal for a wide range of advanced optoelectronic applications, including high-mobility photodetectors, transistors, and logic circuits.[7,8] The realization of vertical and lateral heterostructures composed of distinct TMD monolayers offers a powerful approach to synergistically enhance their functionalities, thereby unlocking new possibilities for device performance. The atomically seamless interfaces inherent to these heterostructures give rise to unique physical properties derived from the distinct crystal symmetries of the individual materials. These properties include robust valley polarization, preserved valley coherence, and the ability to selectively tune the valley magnetic moment, collectively enabling novel electronic and optoelectronic phenomena.[9] Lateral heterostructures with edge contacts enable more efficient tuning of band offsets compared to vertical heterostructures, primarily due to the increased spatial separation between the constituent materials.[10] Moving beyond traditional mechanical exfoliation methods for creating artificial heterostructures, chemical vapor deposition (CVD) has emerged as an important tool for the synthesis of 2D heterostructures. CVD provides pristine

The ORCID identification number(s) for the author(s) of this article can be found under https://doi.org/10.1002/adfm.202512962

DOI: 10.1002/adfm.202512962

P. Vashishtha, A. K. Verma, S. P. Giridhar, T. Gupta, M. Sehrawat, V. Aggarwal, D. Sharma, T. Ahmed, I. H. Abidi, S. Walia
Centre for Opto-electronic Materials and Sensors (COMAS)
School of Engineering
RMIT University
124 La Trobe Street, Melbourne, Victoria 3001, Australia
E-mail: irfan.haider.abidi@rmit.edu.au; sumeet.walia@rmit.edu.au

interfaces, essential for high surface energy transfer efficiency, and is better suited to meet the demands of practical device applications.[11,12] A lateral hetero-interface formed by monolayers of 2D materials with distinct chemical potentials and crystalline orientations leads to an enhanced charge carrier density, owing to the epitaxial nature of the interface, which is pivotal for optoelectronic device performance.[13] Therefore, lateral heterostructures synthesized via CVD hold immense potential for achieving optoelectronic properties and are currently a focal point of extensive research.[14]

Although numerous monolayer TMD heterojunctions have been successfully synthesized, demonstrating optoelectronic properties,[15] current research increasingly focuses on the photogalvanic effects within these materials to identify the most promising heterostructure candidates. This growing interest is driven by the well-established understanding that the photogalvanic effect, induced under illumination, plays a crucial role in modulating the resulting photocurrent.[16,17] First-principles calculations have shown that the photogalvanic effect is particularly pronounced in intrinsic semiconductors, owing to their strong light-matter interactions and efficient separation of electron-hole pairs.[18] Moreover, previous studies have demonstrated that the WS_2-MoS_2 lateral heterostructure exhibits a unique electronic structure that effectively separates charge carriers.[19] Additionally, it is reported that the energy conversion efficiency of the WS_2-MoS_2 heterojunction can be significantly enhanced under uniaxial strain, with tensile strain further improving its optoelectronic performance.[20] Although a range of optoelectronic devices based on WS_2-MoS_2 lateral heterostructure have been studied to date,[21–25] the specific role of the epitaxial interface in modulating carrier density and enhancing optoelectronic properties within monolayer heterostructures remains poorly understood.

In this work, we synthesized monolayer WS_2-MoS_2 lateral heterostructures using an optimized single-step low-pressure CVD (LPCVD) process, achieving an atomically seamless, low-disorder interface through sequential edge-epitaxial growth and strategic placement of precursors. Our LPCVD method produces active, unsaturated edge bonds, enabling precise edge-epitaxial growth by reducing oxygen passivation.[26] We systematically investigated the band structure and the pivotal role of the heterointerface in enhancing optoelectronic performance. Our results demonstrate that the atomically seamless interface, enabled by precise control of growth conditions, increases the charge carrier density twofold and facilitates efficient charge separation, driven by a type-II band alignment and a strong interfacial electric field (≈50 mV μm^{-1}). This leads to a enhancement in device performance compared to bare monolayer-based devices. Specifically, the fabricated photodetector exhibit a broadband spectral response from ultraviolet to near-infrared, achieving a photoresponsivity of 1850 mA W^{-1} under 565 nm illumination at 0.1 mW cm^{-2}, representing an enhancement of up to ≈200% over their bare counterparts. Furthermore, the devices demonstrate a low noise equivalent power (NEP) of 1.9×10^{-15} $WHz^{-1/2}$, a high external quantum efficiency (EQE) of 407%, and a detectivity (D) of 4.36×10^{11} Jones, outperforming many reported MoS_2-WS_2-based photodetectors.[27,28] Moreover, compare to recent studies on WS_2-MoS_2 lateral heterostructures,[29] our work uniquely highlight the role of charge transport parallel to the heterointerface, enabled by the parallel electrode configuration, which maximizes the contribution of the interface's engineering effects. Kelvin probe force microscopy (KPFM) and second-harmonic generation (SHG) imaging provide direct experimental evidence of a localized electric field and enhanced nonlinear optical response at the heterointerface, elucidating their critical influence on charge carrier dynamics and broadband photodetection (285–850 nm). These findings address a key knowledge gap by demonstrating how interface engineering, particularly the reduction of interfacial defects and strain, enhances optoelectronic performance beyond what is achievable with conventional CVD-grown heterostructures, ensuring a seamless, defect-minimized interface, as confirmed by structural and optical studies. The study underscores the potential of WS_2-MoS_2 lateral heterostructures for next-generation optoelectronic devices and establishes interface engineering as a powerful strategy for realizing high-performance 2D material interfaces.

P. Vashishtha
Department of Electrical Engineering and Computer Science
University of Arkansas
Fayetteville, AR 72701, USA

P. Vashishtha, A. K. Verma, M. Sehrawat, V. Aggarwal, D. Sharma, G. Gupta
Academy of Scientific and Innovative Research
CSIR-HRDC Campus
Ghaziabad, Uttar Pradesh 201002, India

C. Kofler, J. Kotakoski
Faculty of Physics
University Vienna
Boltzmanngasse 5, Vienna 1090, Austria

A. K. Verma
Light Technology Institute
Karlsruhe Institute of Technology (KIT)
76131 Karlsruhe, Germany

J. O. Tollerud, J. A. Davis
Optical Sciences Centre
Swinburne University of Technology
Hawthorn, Victoria 3122, Australia

N. S. L. Dissanayake, Y. Lu
School of Engineering
ANU College of Systems & Society
Australian National University
Canberra, ACT 2601, Australia

E. L. Mayes, B. J. Murdoch
RMIT Microscopy and Microanalysis Facility
RMIT University
Melbourne 3000, Australia

D. Sharma, G. Gupta
CSIR National Physical Laboratory
Dr. K.S. Krishnan Road, New Delhi 110012, India

2. Results and Discussion

2.1. Characterization of WS_2-MoS_2 Lateral Heterointerface

WS_2 and MoS_2 have similar crystal structures and compatible lattice constants, making them ideal candidates for the growth of monolayer lateral heterostructures. Their matching crystal lattices facilitate the formation of high-quality interfaces. The lateral heterostructure is achieved through a single-step CVD growth process.[3,30] In this method, the second material epitaxially nucleates and grows at the edges of the first material,

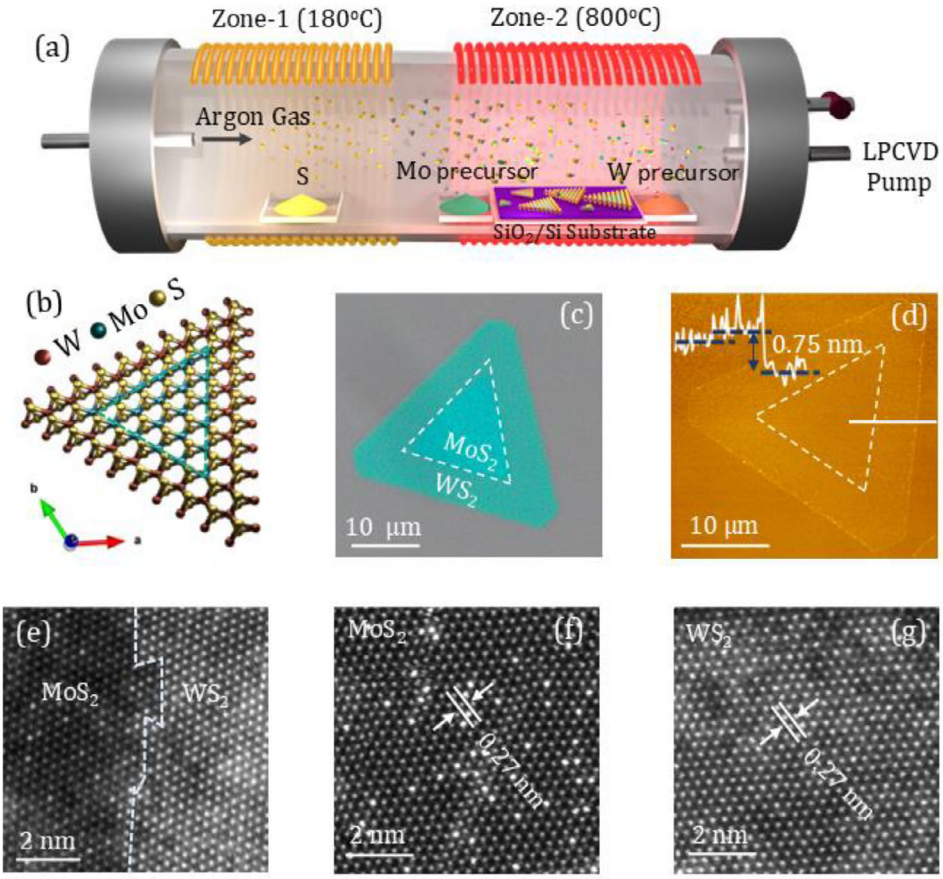

Figure 1. a) Schematic of the CVD process for growing the monolayer MoS_2-WS_2 lateral heterostructure. b) Atomic model of the monolayer WS_2-MoS_2 lateral heterostructure. c) Optical image of a monolayer MoS_2-WS_2 lateral heterostructure. d) AFM height profile image with corresponding thickness data. High-resolution STEM Z-contrast image of area of e) the interface between MoS_2 (left) and WS_2 (right), f) of MoS_2, and g) for WS_2.

resulting in a seamless and defect-free interface. **Figure** 1a illustrates the schematic of the LPCVD growth process for the MoS_2 and WS_2 lateral heterostructure. Detailed methodologies for this process are provided in the experimental section. Figure 1b depicts the atomic structure of the WS_2-MoS_2 lateral heterostructure. In this heterostructure, the central single crystal of a triangular MoS_2 domain is coherently bonded to the adjacent WS_2 regions via covalent bonding, ensuring robust and stable interlayer connections. The monolayer MoS_2-WS_2 lateral heterostructure exhibits regular triangular shapes, as shown in the optical image (Figure 1c). The MoS_2 regions are laterally connected to the peripheral WS_2, resulting in a predominantly triangular geometry with seamless heterointerfaces. During growth, MoS_2 single crystals nucleate first, forming triangular grains, followed by the nucleation of WS_2 at the edges of MoS_2 triangular flakes through edge-epitaxial CVD growth.[3] The typical size of the heterostructure flakes is ≈30 μm, comparable to other reported lateral heterostructures.[21,30] AFM measurements were used to determine the thickness of the heterostructure as shown in Figure 1d, which is ≈0.75 nm across the MoS_2-WS_2 heterostructure, indicating a monolayer thickness throughout the heterostructure. The thickness of the outer material is slightly higher than that of the inner material, with MoS_2 on the inside measuring ≈0.7 nm (Figure S1a, Supporting Information)[31] and WS_2 on the outside measuring ≈0.75 nm (Figure S1b, Supporting Information). We utilized scanning electron microscopy (SEM) and high-resolution transmission electron microscopy (HRTEM) to obtain detailed structural information on the as-grown monolayer lateral heterostructure. These techniques allowed us to analyze the atomic registry at the interface of the lateral heterostructure. Details of the SEM measurement data of the monolayer heterostructure are shown in Figure S1c (Supporting Information), revealing the sharp interface of the lateral monolayer heterostructure. Moreover, the HRTEM images presented key insights into the atomic structure and interface characteristics of the lateral heterostructure of monolayer MoS_2 and WS_2. The HRTEM image in Figure S1d (Supporting Information), SI provides a Z-contrast view of the lateral interface, where tungsten (W) atoms exhibit significantly higher image intensity than molybdenum (Mo) atoms. This distinct contrast highlights the seamless integration and abrupt transition between the MoS_2 and WS_2 lattices, characterized by a sharp boundary within atomic rows. To further resolve the interface structure, we employed high-resolution aberration-corrected annular dark-field (HAADF) scanning transmission electron microscopy (STEM). The Z-contrast image in Figure 1e shows that the ADF signal scales $\sim Z^{1.7}$, allowing for a clear distinction among W (Z,74), Mo (Z,42), and S (Z,16) atoms based on image intensity,

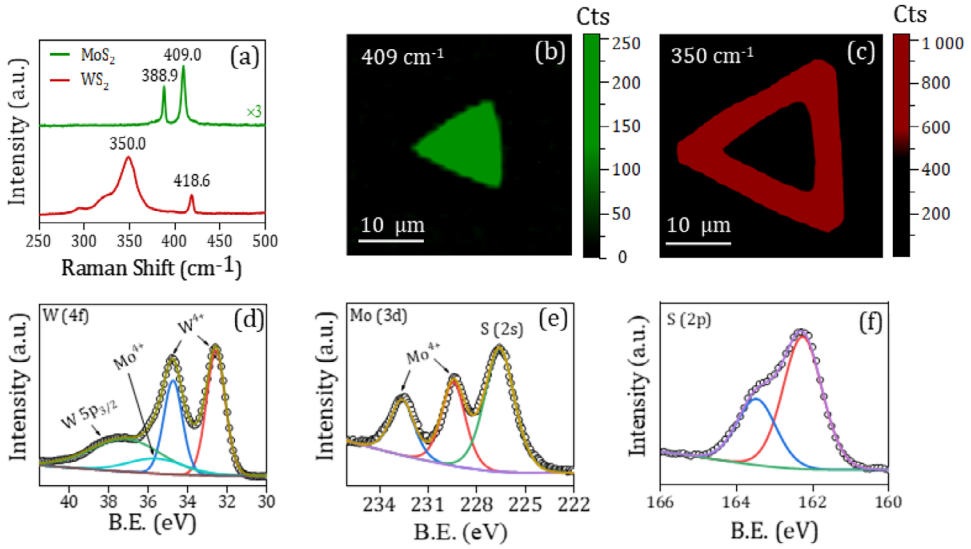

Figure 2. a) Raman spectra obtained from the central MoS_2 region and the outer WS_2 region. Raman mapping images of b) MoS_2 at 409 cm^{-1} and c) WS_2 at 350 cm^{-1}. XPS core level spectra of d) W 4f, e) Mo 3d, and f) S 2p for the grown lateral monolayer heterostructure.

the observation suggest that the interface is atomically seamlessly connected, following a zigzag configuration (depicted by light blue dotted line), in accordance with Gong et. al. recent work.[30] The lateral WS_2-MoS_2 junction reveals that more than 90% of the W and Mo atoms are located at the interface with a slightly higher density of W atoms in MoS_2, each bonded to two sulfur atoms and one neighboring transition metal atom (W-Mo or Mo-W), forming a coherent heterojunction. No structural instabilities, phase transitions, dislocations, or grain boundaries were observed. All atoms conform to a single MX_2 honeycomb lattice across the interface, exhibiting a sixfold symmetry pattern, which indicates minimal lattice distortion and confirms the formation of a near-perfect lateral epitaxial interface. The atomic resolution STEM image in Figure 1f focuses on the MoS_2 region. The lattice fringes have a spacing of ≈0.27 nm, corresponding to the (100) plane of MoS_2. Similarly, the atomic resolution STEM image in Figure 1g depicts the WS_2 region. The lattice spacing, again ≈0.27 nm, matches the expected interplanar distance for the (100) planes of WS_2. The images reveal that the WS_2 and MoS_2 domains form a continuous D_{3h} symmetrical hexagonal monolayer lattice with identical crystal orientation across the interface. This atomically coherent interface supports the mechanism of lateral epitaxial growth, wherein the WS_2 monolayer nucleates and extends directly from the MoS_2 edges while maintaining a perfect atomic lattice arrangement. The matching lattice parameters between the MoS_2 and WS_2 suggest successful edge epitaxial growth, which is key for the seamless integration of these materials in the lateral monolayer heterostructure.

Raman measurements were conducted to investigate the structural properties of the monolayer MoS_2-WS_2 lateral heterostructure. Raman spectra extracted from different positions of the flake (center and edge) are shown in **Figure 2a**. The upper spectrum corresponds to the center of the flake, while the lower spectrum corresponds to the edge. The spectra from the center region show two major peaks at 388.9 and 409 cm^{-1}, while after deconvoluting the data (Figure S2a, Supporting Information) reveal four peaks correspond to characteristic Raman modes of MoS_2: the E^1_{2g} mode at 388.9 cm^{-1} and the A_{1g} mode at 408.7 cm^{-1} and the peak separation is found to be $\Delta = 19.8$ cm^{-1}, confirms the MoS_2 monolayer.[32] The other two peaks are related to the longitudinal and out-of-plane optical branches. The edge region exhibits two major Raman peaks at 418.6 and 350 cm^{-1}, corresponds to WS_2, while the deconvoluted data in Figure S2b (Supporting Information), SI, reveal six distinct peaks. The fitting determined the positions of the in-plane mode E^1_{2g} (Γ) at 356.5 cm^{-1} and the out-of-plane mode A^1_g (Γ) at 418.6 cm^{-1}. The separation between these peaks is $\Delta = 62.1$ cm^{-1}, consistent with the WS_2 monolayer range of 61.5–62.4 cm^{-1}.[33] Figure 2b,c present Raman mappings corresponding to the peak positions at 409 cm^{-1} for MoS_2 and 350 cm^{-1} for WS_2, respectively. These mappings exhibit the homogeneity and bright contrast variations in the central triangular region of MoS_2 and the lateral material outer triangular shell of WS_2. This confirms the successful formation of the monolayer MoS_2-WS_2 lateral heterostructure. Furthermore, the Raman data obtained from the interface of the lateral heterostructure, as depicted in Figure S2c (Supporting Information), reveal a very low additional peak at ≈416 cm^{-1}. This peak corresponds to the A_1(M) mode of the WS_2 monolayer. The low intensity of this peak is attributed to the sharp interface of the WS_2 monolayer with the MoS_2.[34] The peak intensities of the longitudinal and out-of-plane optical branches, indicative of minimal sulfur vacancies in the MoS_2 monolayer, are the same as at the interface, as detailed in Figure S2d (Supporting Information). Moreover, X-ray Photoelectron Spectroscopy (XPS) was employed to analyze the detailed chemical composition of the WS_2-MoS_2 lateral heterostructure. Figure 2d shows the W (4f) spectrum, while Figure 2e,f present the Mo (3d) and S (2p) deconvoluted spectra of the heterostructure, respectively. The core level spectra in Figure 2d reveal three distinct valence states, W^{4+} associated with the W $4f_{7/2}$ peak, while Mo^{4+} corresponds to the Mo $4p_{3/2}$, and an additional peak attributed to the W $5p_{3/2}$ state. W has distinct chemical states in the observed peaks: the W^{4+} valence state

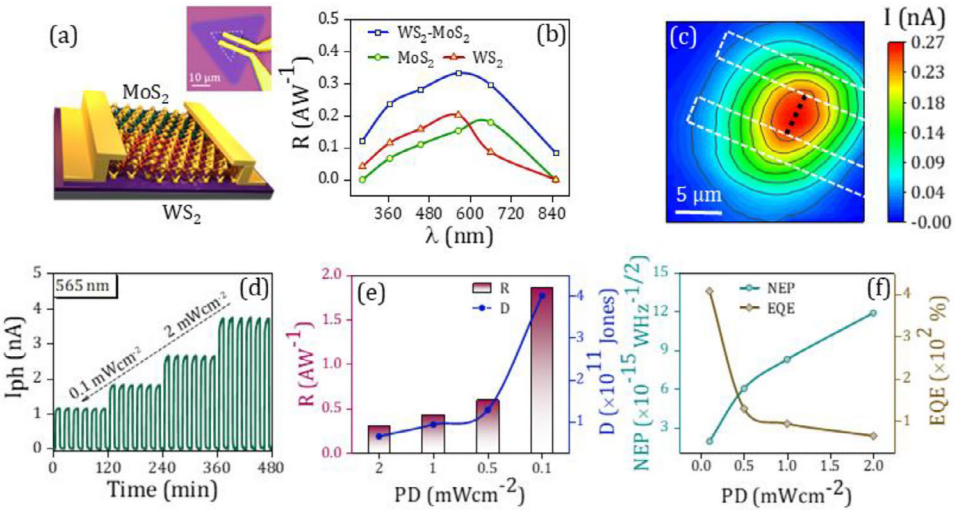

Figure 3. a) Schematic of the two-terminal devices, inset: optical image of a typical photodetector device, b) spectral response comparing with its bare counterparts, c) photocurrent mapping of the fabricated lateral heterostructure-based device. Power correlated d) photo-switching cycle, e) responsivity & detectivity, f) noise equivalent power and the efficiency under 565 nm illumination laser at an applied bias of 1 V.

associated with W 4f in hexagonal WS_2. The XPS core-level spectrum of Mo (3d), shown in Figure 2e, reveals three characteristic peaks. Two of these peaks correspond to Mo^{4+}, confirming the presence of MoS_2 in the sample; an additional peak in the same spectrum also exhibits the S 2s peak. For the S 2p core level of the heterostructure, two distinct peaks are observed (S $2p_{1/2}$) and (S $2p_{3/2}$), corresponding to the S atoms in the monolayer heterostructure, as depicted in Figure 2f. Furthermore, a semiquantitative analysis was conducted to determine the elemental ratios, revealing an atomic ratio of S/(Mo + W) of ≈1.98,[35] closely matches the stoichiometric balance of monolayer MoS_2 and WS_2.

2.2. Photoresponse Measurements for WS_2-MoS_2-Based Devices

To elucidate the effect of the sharp WS_2-MoS_2 interface on optoelectronic properties, two-terminal electrodes with an active area of 60 μm^2 (Au/Cr: 100/10 nm) were fabricated. The schematic and microscopy image of the fabricated device are depicted in **Figure** 3a, showing interfaces marked by a dashed line. The fabricated heterostructure-based device demonstrated a lower dark current compared to the individual MoS_2 and WS_2 monolayers, as depicted in Figure S3a (Supporting Information). This reduction in dark current can be attributed to the unique configuration of the heterostructure, where three distinct pathways are available for the flow of charge carriers, effectively forming a parallel circuit.[36] This parallel arrangement facilitates a more efficient charge transport mechanism, thereby reducing the overall dark current in the device.[36] Moreover, the lower dark current of the fabricated heterostructure-based device is attributed to the type-II band alignment and depletion region at the WS_2-MoS_2 interface, which creates a built-in electric field (discussed later) that suppresses thermally generated carriers in the dark state. The atomically seamless interface further reduces defect-related leakage currents. The distinct charge transport pathways at MoS_2, WS_2, and interface regions, facilitated by epitaxial growth, increase the effective resistance to dark current flow compared to bare material devices, resulting in a reduction in dark current. Figure 3b illustrates the spectral response (responsivity—R as a function of incident light wavelength—λ) for the monolayer WS_2-MoS_2 lateral heterostructure, along with the bare WS_2 and MoS_2 monolayers, which is calculated using the wavelength-correlated photo-switching as shown in Figure S3b–d (Supporting Information). The heterostructure-based device shows enhanced responsivity across the spectral range, achieving a peak value at 565 nm illumination. Moreover, the fabricated device displays a broader spectral range for the heterostructure than its bare counterparts, especially in the infrared region. To investigate the origin of the enhanced photoresponse of the device, photocurrent mapping was performed under an optical power density of 20 mW cm^{-2} using a 660 nm laser to comprehensively assess the spatial distribution of photocurrent across the heterostructure, as illustrated in Figure 3c. In this mapped image, the white dotted line defines the position of the electrodes, while the black dotted line marks the interface of the lateral WS_2-MoS_2 heterostructure. The spatial map provides a detailed visualization of the photocurrent distribution, measured in nanoamperes (nA), across the heterostructure. Notably, the photocurrent is maximized at the interface region, indicating a significant enhancement in charge separation and transport at the heterostructure interface. This observation suggests that the lateral hetero interface facilitates more efficient photocarrier generation and collection than the bare MoS_2 and WS_2 monolayer regions. The enhanced photocurrent at the interface underscores the importance of the lateral monolayer heterostructure in optoelectronic performance. To thoroughly evaluate the photoresponse of the device, we conducted power-dependent measurements. Following the power correlated current–voltage (I–V) analyses (depicted in Figure S4a, Supporting Information), the systematic assessments of the transient photoresponse (I—T) through repeated on/off cycles, each lasting 600s, were performed. The tests were performed under varying optical radiation intensities, ranging from 2 to 0.1 mW cm^{-2}, with a constant 1 V applied bias, as shown in Figure 3d. The results confirm that the

detector is durable throughout multiple cycles, even at the low intensity of 0.1 mW cm^{-2}. Moreover, the photocurrent is a positive function of the illumination optical power density (PD), which increases with increasing intensity. This behavior is due to fewer photogenerated carriers being available at lower intensities, reducing radiative recombination. Additionally, the presence of trap states significantly influences the photocurrent, especially at lower power levels. This relationship is described by the power law equation $I_{ph} = P^{\gamma}$, where γ indicates the effect of these trapping processes.[37,38] Subsequently, a sub-linear fitting of the experimental data was performed to determine the exponent γ, as shown in Figure S4b (Supporting Information). The observed deviation of γ from unity indicates the presence of localized trap states in the grown heterostructure, likely due to sulfur vacancies, which influence the recombination dynamics. The switching speed of the device was also calculated, with rise and decay times recorded at 53 and 31 s, respectively, as illustrated in Figure S4c (Supporting Information). Additionally, for the fabricated lateral WS_2-MoS_2 heterostructure-based device, several key performance metrics were calculated under varying power-dependent conditions. These include R, D, EQE, and NEP, providing a comprehensive evaluation of the photodetector performance.[39] The responsivity of the fabricated detector exhibits an inverse correlation with incident light intensity, as illustrated in Figure 3e. This behavior is attributed to trap states, which include a vacancy within the interface. Under low light intensity, these trap states capture the photogenerated electrons, reducing the recombination of electron-hole pairs. At higher illumination intensities, the capacity of trap states to capture photogenerated electrons becomes increasingly limited. As a result, the device exhibits enhanced responsiveness under lower light conditions.[40] The zenith R-value of the fabricated heterostructure-based detector was calculated to be 1850 mA W^{-1} under illumination at a wavelength of 565 nm. Similarly, the specific detectivity follows the same trend as the responsivity, reaching a maximum value of 4.36×10^{11} Jones at a lower illumination power density. Other key performance parameters, such as the EQE and NEP, were also evaluated, as shown in Figure 3f. The EQE increased with decreasing light intensity, while the NEP exhibited an inverse relationship. The optimal values for NEP and EQE were found to be 1.9×10^{-15} $WHz^{-1/2}$ and 407%, respectively, under an optical power density of 0.1 mW cm^{-2} at 565 nm illumination. These results highlight the device's exceptional performance in terms of merits, including efficiency in converting incident light into electrical signals. In diode and p-n junction-based optical detectors, efficiency is typically higher than 100%, as each incident photon generates more than one electron-hole pair contributing to the photocurrent. However, in photoconductive detectors like our WS_2-MoS_2 lateral heterostructure, EQE can exceed 100% due to photoconductive gain. This gain results from prolonged carrier lifetimes, density, and mobility facilitated by an atomically sharp monolayer heterointerface, allowing multiple charge carriers to contribute to the photocurrent per absorbed photon. Thus, the fabricated device exhibits an EQE exceeding 100%, demonstrating its superior ability to convert incident photons into electrical signals.[41] This phenomenon can be attributed to several key factors, particularly the seamless characteristics of lateral heterointerface growth. The epitaxial lateral configuration of the heterostructure promotes higher interactions between the incident photons and the interface of the grown structure. These repeated photon-material interactions significantly enhance the probability of photon absorption and subsequent electron-hole pair generation. As a result, the lateral hetero-interface serves as a platform for increased photon-matter coupling, leading to a more efficient photoresponse. This enhanced interaction is key in optimizing the device's overall performance, as it allows for greater utilization of the incident light, thereby improving the efficiency of photodetection and the generation of charge carriers.[42] The performance of the fabricated lateral hetero-interface device was systematically compared with previously reported monolayer heterostructure photodetectors, as summarized in Table S1 (Supporting Information). This comparison reveals that the photodetection capabilities of our device significantly surpass those of earlier designs, exhibiting superior photoresponse characteristics.

2.3. Electro-Atomic Dynamics at the WS_2-MoS_2 Heterointerface

Lateral epitaxial heterointerfaces in atomically thin materials, characterized by seamless connectivity, strong coupling, and atomically junctions, present a significant advantage by enabling efficient charge carrier transport while preserving the intrinsic properties of the constituent materials. Unlike vertical heterostructures, where interlayer coupling and stacking orientation can introduce variations in electronic states, lateral heterojunctions ensure robust band alignment and minimized interfacial scattering, thereby enhancing carrier mobility.[43] Thus, the higher photocurrent generation at the interface of monolayer lateral heterostructures can be attributed to optical light absorption driven by the seamless interface, band alignment, interfacial electric field, and opto-atomic carrier dynamics, to solidify the potential in highly efficient optoelectronic applications. To understand the effect of the interface on the charge carrier mechanism. The PL measurement of the fabricated heterostructure is performed; the corresponding results are shown in **Figure** 4a. The observation revealed that the MoS_2 and WS_2 peaks are distinct, located at ≈1.84 and ≈1.92 eV, respectively, representing each material's characteristic direct near-band edge emission peaks.[44,45] The PL intensity at the interface (blue curve) is noticeably reduced compared to the individual materials, suggesting quenching effects likely due to band alignment and non-radiative recombination processes at the heterojunction. Moreover, the PL spectra at the interface show unshifted data, exhibiting a stressed relaxed epitaxial interface. In type-II band alignment, the conduction band minimum of one material aligns lower than the other, while the valence band maximum of the first material aligns higher. This staggered structure encourages electrons and holes to separate between the two materials. When charges are spatially separated, they have fewer opportunities to recombine radiatively, leading to non-radiative recombination pathways that diminish PL intensity.[46] The valence band spectra (shown in Figure 4b) show the position of the Fermi level relative to the valence band edge of WS_2 and MoS_2, observed 0.14 ± 0.02 eV shift in the valence band, along with the conduction band offset of 0.22 ± 0.02 eV, suggests a type-II band alignment (Figure 4c) at the interface. The WS_2-MoS_2 heterostructure exhibits a calculated bandgap of 1.70 ± 0.02 eV, with a Q–K energy spacing of ≈110 meV.[47]

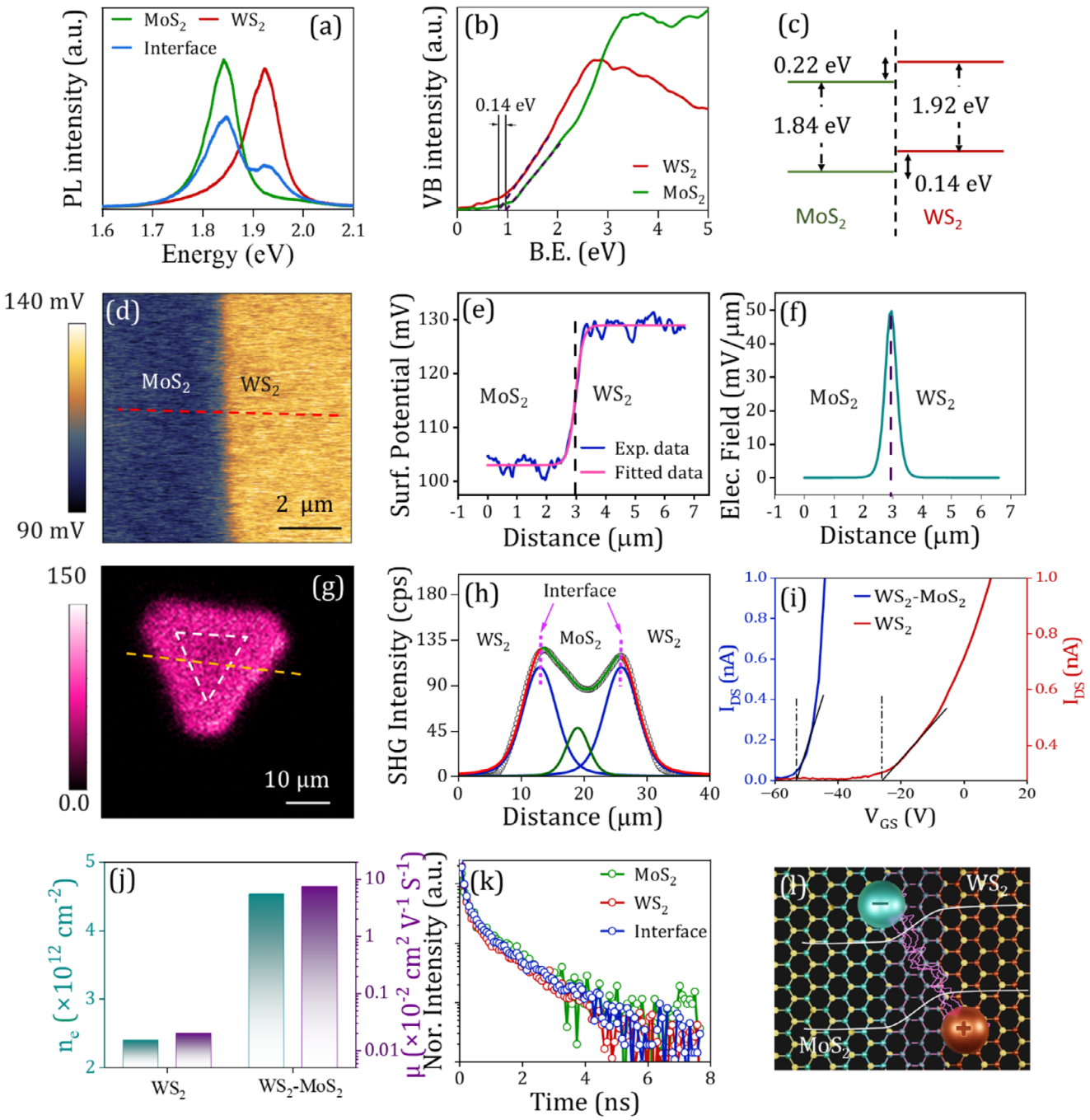

Figure 4. a) PL spectra of the interface compared to its bare counterparts, b) XPS valence band spectra of MoS_2 and WS_2, c) calculated band alignment diagram, d) KPFM surface potential distribution image, e) surface potential profile across the interface corresponding to red line, and f) derived electric field distribution of the heterostructure g) SHG intensity mapping image, h) represents their line profile along the yellow dashed line, i) Charge Transfer characteristics of the fabricated FET, j) comparison of field-effect electron mobility, carrier density, k) TRPL spectra of the lateral heterointerface compared with its bare counterpart, and l) schematic of a lateral heterointerface showing spatially separated charge-transfer excitons.

The valence band maximum arises from contributions of the d-orbitals of W and Mo, as well as the p-orbitals of S, whereas the d-orbitals of Mo primarily dominate the conduction band minimum. Hong et al.[48] reported that charge transfer through the lateral MoS_2-WS_2 type-II heterojunctions occurs within just 50 fs, indicating highly efficient charge separation despite the significantly larger exciton binding energy. This fast charge separation is primarily driven by strong Coulomb interactions, which stabilize charge transfer excitons and facilitate interlayer carrier dynamics. Absorption spectroscopy (see Figure S4d, Supporting Information) reveals a pronounced modification of excitonic transitions in WS_2 upon optical excitation of MoS_2, which

possesses a wider bandgap. This observation provides direct evidence of efficient charge separation within the photoexcited heterostructure. Upon photon absorption, electron-hole pairs are initially generated in the MoS_2. However, due to the type-II band alignment, holes rapidly transfer to the WS_2 layer while electrons remain confined in MoS_2. The spatial separation of charge carriers induces a strong transient absorption response at the heterointerface, attributed to the sharper excitonic resonances and pronounced photo-bleaching effects of Pauli blocking.[48] This process effectively enhances photocurrent generation.[49]

Moreover, the electronic properties of the lateral heterostructure were also investigated using Kelvin probe force microscopy (KPFM) to elucidate the photoresponse mechanism. The surface potential distribution of the heterostructure, shown in Figure 4d, reveals that the surface potential of MoS_2 (on the left) is lower than that of WS_2 (on the right) due to their differing work functions. A clear depletion region is observed at the lateral interface. Figure 4e displays the surface potential distribution along the direction indicated by the red-dotted line in Figure 4d, with the surface potentials measured at 102 mV for MoS_2 and 129 mV for WS_2. Additionally, the valence band offset of 140 mV, along with a Fermi level difference of ≈27 mV between WS_2 & MoS_2, and a depletion region width of ≈1.8 µm across the heterojunction, as shown in Figure 4b,e, confirm the formation of a monolayer junction. In this heterostructure, WS_2 behaves as an n-type semiconductor and MoS_2 as an n^+-type semiconductor. The measured built-in potential across the heterojunction effectively enhances the separation of photogenerated electron-hole pairs, facilitating efficient charge separation and transport. The surface potential in Figure 4e is well fitted by Equation S7 (Supporting Information) to calculate the built-in electric field distribution of the heterostructure by differentiating the fitting profile in Figure 4f, where a maximum electric field of ≈50 mV μm^{-1} exists at the midpoint of the depletion region. The strong electric field at the interface enables efficient spatial separation and directional transport of charge carriers along the lateral interface. This guided in-plane transport enhances charge collection and reduces recombination, resulting in more effective charge carrier dynamics than independently in WS_2 or MoS_2 monolayers. As a result, the electric field at the heterojunction interface plays a pivotal role in boosting device performance, enabling faster, more efficient charge transport and improved photoresponse compared to the bare materials. The high electric field observed at the interface is attributed to the seamless and low-disorder epitaxial interface. Moreover, Sousa et al.[50] demonstrated that the electric field at the interface, denoted as $E_{int} = \frac{E_{Mo}+E_W}{\sqrt{2}}$ is directly correlated with the nonlinear optical intensity through the relation $E \alpha |I|^2$ where I represent the SHG intensity. The SHG intensity is expressed as $I = \frac{I_{Mo}}{2} + \frac{I_W}{2} + \epsilon\sqrt{I_{Mo}I_W}$, where $\epsilon = 1$, owing to the same crystallographic orientation of the materials in the lateral heterostructure. SHG measurements were performed to investigate the lateral interface further. The SHG mapping of the monolayer lateral heterostructure is shown in Figure 4g, while the corresponding line profile, extracted along the yellow line, is presented in Figure 4h. The deconvoluted line profile (obtained by fixing the area and intensity of both the interfacial peaks displayed by the blue spectra) reveals that the SHG intensity at the interface is significantly enhanced compared to the bare domains of the monolayer materials. Additionally, a secondary peak appears near the center of the interface, which could be attributed to the presence of nucleation seeds of the monolayer heterostructure. These observations suggest that the SHG response exhibits a pronounced and localized enhancement at the lateral interfaces, confirming the strong interfacial coupling between the two materials.

Furthermore, to assess the charge carrier transport at the interface of the devices, employ top contacts serving as source and drain with heavily doped p-type silicon (p++) acting as a global back gate, allowing operation in a three-terminal field-effect transistor (FET) device. The electrical characteristics of interface devices were compared to those of monolayer WS_2 grown outside the lateral heterostructure, as depicted in Figure 4i. Both device types exhibit n-type behavior with negative threshold voltages (V_T). However, the heterostructure device exhibits a more pronounced threshold voltage shift ($V_T \approx -53$ V) compared to the monolayer WS_2 device ($V_T \approx -26$ V), indicating stronger n-doping in the heterostructure. This shift is likely due to charge transfer at the heterointerface, which elevates the intrinsic carrier concentration. Our calculations, shown in Figure 4j, reveal a field-effect carrier density (n_e) of 4.55×10^{12} cm^{-2} in the heterostructure device, surpassing that of the WS_2 device ($n_e = 2.41 \times 10^{12}$ cm^{-2}). Additionally, the heterostructure devices demonstrate an enhanced field-effect mobility compared to the bare WS_2 monolayer. This improved mobility arises from both the increased carrier concentration and superior contact properties at the heterointerface.

Time-resolved photoluminescence (TRPL) was measured in the monolayers and interface regions, as shown in Figure 4k. At the nanosecond time scales probed in this measurement, the dynamics are predominantly dictated by defect lifetimes. The results indicate no significant deviation in the interface region compared to the MoS_2 and WS_2 domains, aligning closely with earlier studies that reported a decay time at the monolayer MoS_2-WS_2 interface is few picoseconds higher than the bare monolayers parts,[48] which is consistent with an epitaxial growth picture where the heterostructure interface is low disorder and epitaxial growth prevails leading to a heterojunction with the strong in-plane covalent bonds[51] and 1D interface widths comparable with the excitonic Bohr radius. The seamless interface of the heterostructure enables strong Coulomb interactions that bind electrons and holes from both materials[52] (discussed earlier); a schematic is depicted in Figure 4l. Furthermore, the small difference in band gaps and exciton energies between MoS_2 and WS_2 minimizes bound charge transfer across the lateral junction, resulting in unique transport behavior along the interface. This can lead to rapid, high-density diffusion, with diffusion coefficients up to three orders of magnitude higher than those in individual layers.[53] This could be attributed to dipole-dipole repulsion and Mott transition effects, which create exciton-like pathways that facilitate efficient charge carrier transport. These effects aid in the efficient separation of charges and control the movement of excitons under the influence of electric fields. As a result, the epitaxial lateral heterointerface holds significant potential for optoelectronic devices due to its strong 1D confinement, high electric field, opto-atomic carrier dynamics and rapid exciton diffusion.

3. Conclusion

This work reveals fundamental insights into atomically sharp boundaries of lateral 2D heterostructures using WS_2-MoS_2 as the model materials. We use this to demonstrate that the CVD growth process successfully produced a seamless lateral heterostructure with an atomically seamless interface. A detailed structural analysis confirmed the monolayer nature of the heterostructure and revealed seamless, coherent interfaces that are key for optimal electronic performance. The photodetector demonstrated photo response, attributed to the type−II band alignment at the WS_2-MoS_2 interface, which enhances charge separation and minimizes recombination losses. The device exhibited a peak responsivity of 1850 mA W^{-1} and a maximum detectivity of 4.36×10^{11} Jones under 565 nm illumination, with a NEP (EQE) 1.9×10^{-15} $WHz^{-1/2}$ (407%), highlighting its ability to convert incident photons into electrical signals efficiently. Surface potential and SHG mapping confirm the presence of interfacial electric fields and a nonlinear response, linking the lateral heterojunction to enhanced photoresponse. The study's findings underscore the potential of lateral WS_2-MoS_2 heterostructures in advancing the development of high-performance optoelectronic devices, particularly in applications requiring broad spectral coverage and high sensitivity.

4. Experimental Section

Growth of Epitaxial Monolayer WS_2-MoS_2 Lateral Heterostructure: Monolayer WS_2-MoS_2 lateral heterostructures were synthesized on 300 nm SiO_2/Si substrates using an optimized single-step LPCVD process in a two-zone furnace (Labec HTFS80) with an 80 mm quartz tube. Compared to atmospheric pressure CVD, which yields oxygen-passivated edges and diffuse interfaces due to ambient oxygen exposure, our optimized LPCVD approach produces active, unsaturated edge bonds, promoting precise edge-epitaxial growth.[26] To enhance nucleation and ensure uniform monolayer growth, substrates were ultrasonically cleaned in acetone, isopropanol, and deionized water, followed by N_2 drying and O_2 plasma treatment (300 s) to increase surface wettability.[54] MoO_3 and WO_3 powders (30 mg each) served as Mo and W precursors, respectively, and were placed on opposite sides of the substrate in temperature zone-2 to minimize cross-contamination, a technique adapted from.[3] Sulfur powder (300 mg) was placed in zone-1, maintained at 180 °C throughout. The chamber was purged with 500 sccm of Ar for 10 min to establish a clean environment, followed by a reduced Ar flow of 70 sccm at 1 Torr to control precursor vapor dynamics. Zone-2 was ramped to 750 °C for 5 min to nucleate triangular MoS_2 grains, followed by a controlled ramp to 800 °C with a 20-min dwell to enable edge-epitaxial WS_2 growth at the MoS_2 domain edges. This sequential growth minimizes intermixing and defect formation, resulting in an atomically seamless interface. Rapid cooling under Ar flow preserved interface quality, reducing thermal-induced defects compared to standard CVD methods.

Material Characterization: Optical images of the as-grown monolayer WS_2-MoS_2 lateral heterostructure and based devices were captured using a Leica microscope. The thickness of the heterostructure was measured with a Bruker Dimension Icon AFM using a Scan Asyst-air tip. Morphological and characterizations, including SEM (FEI Verios), HRTEM, and SAED patterns, were performed with a JEOL JEM-F200 CFEG TEM at 200 kV. STEM characterization was performed using a Nion UltraSTEM 100 device at an electron energy of 60 keV and a convergent semi-angle of ≈34 mrad, after introducing the sample to ultra-high vacuum conditions and heating to ≈180 °C for 8 h. A HAADF detector with a semi-angular range of 80–300 mrad was used for imaging. The HAADF-STEM images were smoothed using a Gaussian filter. The elemental composition of WS_2 and MoS_2 was analyzed using a Kratos AXIS Supra XPS spectrometer with a 1486.7 eV (Al Kα) X-ray source. UV–vis characteristics were measured with a CRAIC Microspectrophotometer, and Raman and PL analysis were conducted using a HORIBA Lab RAM Raman spectrometer with a 532 nm laser. The high-resolution surface potential map at the MoS_2-WS_2 interface was performed using Scanning Kelvin Probe Force Microscopy (SKPFM) on an MFP-3D Infinity instrument (Oxford Instruments, Asylum Research, Santa Barbara, CA, USA). The measurements were done using a PtIr-coated, antimony-doped silicon cantilever (SCM-PIT-V2) from Bruker, with a spring constant of 3 N m^{-1} and a resonance frequency of 75 kHz. SHG measurements were performed using a Zeiss 780 confocal microscope at room temperature. The excitation source was a tunable Ti: sapphire laser with a pulse duration of 150 fs and an 80 MHz repetition rate. The sample was illuminated through a 50× confocal objective lens (numerical aperture, 0.85). A laser wavelength of 900 nm was employed for the SHG experiments. The SHG signal was validated by confirming that it is half the excitation wavelength.

Device Fabrication: Using standard photolithography, two-terminal lateral devices were fabricated on as-grown WS_2-MoS_2 heterostructures on a 300 nm SiO_2/Si substrate. AZ5214E photoresist was spin-coated, and source/drain electrodes were patterned with a maskless aligner (MLA−150). After development, 100/10 nm Au/Cr contacts were deposited via electron beam deposition (Kurt L. Lasker, PVD−75) at a base pressure of 6×10^{-7} Torr, followed by lift-off in acetone.

Opto-Electronic Measurements: Optoelectronic measurements were performed using a Keysight 2901A#02 source measurement unit on a Linkam stage probe station under ambient conditions (room temperature, in air). The devices were illuminated with uncollimated monochromatic LEDs (Thorlabs Inc., emitter size: 1–2.5 mm, larger than the active area of the device) spanning a wavelength range of 285 to 850 nm. The power intensity, calibrated with a commercial photodetector (Newport Corporation), was varied to assess the photodetection capabilities.

Supporting Information

Supporting Information is available from the Wiley Online Library or from the author.

Acknowledgements

This research was conducted partly at the Micro Nano Research Facility (MNRF) at RMIT University, within Victoria's Australian National Fabrication Facility. The authors thank the MNRF and RMIT Microscopy and Microanalysis Research Facility staff for their technical assistance. S.W. and I.H.A. acknowledge support from the Australian Research Council Discovery Project DP220100020 and DP240100145 (S.W.). P.V. expresses gratitude to RMIT for financial support through the RMIT-AcSIR fellowship. S.P.G. acknowledges scholarship support through the National Intelligence and Security Research Grant (NS210100083) and the Department of Defence Science and Technology. S.W. and T.A. acknowledge support from the Office of National Intelligence (NI230100026). The authors also acknowledge the Director of CSIR-NPL and AcSIR India for their enduring support.

Conflict of Interest

The authors declare no conflict of interest.

Data Availability Statement

The data that support the findings of this study are available from the corresponding author upon reasonable request.

Keywords

2D materials, lateral heterointerface, monolayer, MoS_2, photoresponse, TMDs, WS_2

Received: May 22, 2025
Revised: August 7, 2025
Published online:

[1] J. Quereda, S. Kuriakose, C. Munuera, F. J. Mompean, A. M. Al-Enizi, A. Nafady, E. Diez, R. Frisenda, A. Castellanos-Gomez, *npj Flex. Electron.* **2022**, *6*, 23.
[2] K. Kang, S. Xie, L. Huang, Y. Han, P. Y. Huang, K. F. Mak, C.-J. Kim, D. Muller, J. Park, *Nature* **2015**, *520*, 656.
[3] X. Duan, C. Wang, J. C. Shaw, R. Cheng, Y. Chen, H. Li, X. Wu, Y. Tang, Q. Zhang, A. Pan, *Nat. Nanotechnol.* **2014**, *9*, 1024.
[4] M.-Y. Li, Y. Shi, C.-C. Cheng, L.-S. Lu, Y.-C. Lin, H.-L. Tang, M.-L. Tsai, C.-W. Chu, K.-H. Wei, J.-H. He, *Science* **2015**, *349*, 524.
[5] A. K. Verma, M. A. Rahman, P. Vashishtha, X. Guo, M. Sehrawat, R. Mitra, S. P. Giridhar, M. Waqar, A. Bhoriya, B. J. Murdoch, *ACS Nano* **2025**, *19*, 3478.
[6] A. R. Rezk, S. Walia, R. Ramanathan, H. Nili, J. Z. Ou, V. Bansal, J. R. Friend, M. Bhaskaran, L. Y. Yeo, S. Srirram, *Adv. Opt. Mater.* **2015**, *3*, 888.
[7] C. Tan, H. Wang, X. Zhu, W. Gao, H. Li, J. Chen, G. Li, L. Chen, J. Xu, X. Hu, *ACS Appl. Mater. Interfaces* **2020**, *12*, 44934.
[8] Y. Wang, C. Du, P. Li, Y. Yang, Y. Xiao, T. Ge, X. Jiang, Y. Liu, H. Gao, K. Li, *ACS Appl. Mater. Interfaces* **2024**, *1*, 29049.
[9] P. K. Sahoo, S. Memaran, F. A. Nugera, Y. Xin, T. Díaz Márquez, Z. Lu, W. Zheng, N. D. Zhigadlo, D. Smirnov, L. Balicas, *ACS Nano* **2019**, *13*, 12372.
[10] C. Herbig, C. Zhang, F. Mujid, S. Xie, Z. Pedramrazi, J. Park, M. F. Crommie, *Nano Lett.* **2021**, *21*, 2363.
[11] Z. Zhang, Z. Huang, J. Li, D. Wang, Y. Lin, X. Yang, H. Liu, S. Liu, Y. Wang, B. Li, *Nat. Nanotechnol.* **2022**, *17*, 493.
[12] Y. Liu, N. O. Weiss, X. Duan, H.-C. Cheng, Y. Huang, X. Duan, *Nat. Rev. Mater.* **2016**, *1*, 16042.
[13] R. Zhang, M. Li, L. Li, Z. Wei, F. Jiao, D. Geng, W. Hu, *Adv. Funct. Mater.* **2021**, *31*, 2102049.
[14] X. Zhou, X. Hu, J. Yu, S. Liu, Z. Shu, Q. Zhang, H. Li, Y. Ma, H. Xu, T. Zhai, *Adv. Funct. Mater.* **2018**, *28*, 1706587.
[15] C. Liu, K. M. M. H Liu, *Nat. Nanotechnol.* **2022**, *17*, 439.
[16] X. Tao, P. Jiang, H. Hao, X. Zheng, L. Zhang, Z. Zeng, *Phys. Rev.* **2020**, *B 102*, 081402.
[17] Y. Gao, Y. Zhang, D. Xiao, *Phys. Rev. Lett.* **2020**, *124*, 077401.
[18] K. Cheng, Y. Guo, N. Han, X. Jiang, J. Zhang, R. Ahuja, Y. Su, J. Zhao, *Appl. Phys. Lett.* **2018**, *2*, 112.
[19] X.-L. Wei, H. Zhang, G.-C. Guo, X.-B. Li, W.-M. Lau, L.-M. Liu, *J. Mater. Chem. A* **2014**, *2*, 2101.
[20] J. Lee, J. Huang, B. G. Sumpter, M. Yoon, *2D Mater.* **2017**, *4*, 021016.
[21] D. Zhao, H. Jiao, C. Chen, Y. Chen, S. Wang, H. Cao, X. Wang, G. Yu, W. Bai, X. Tang, *Adv. Opt. Mater.* **2023**, *11*, 2300709.
[22] J. Park, J. O. Kim, S.-W. Kang, *Sci. Rep.* **2024**, *14*, 6922.
[23] X. Zhang, L. Huangfu, Z. Gu, S. Xiao, J. Zhou, H. Nan, X. Gu, K. Ostrikov, *Small* **2021**, *17*, 2007312.
[24] P. K. Sahoo, S. Memaran, Y. Xin, L. Balicas, H. R. Gutiérrez, *Nature* **2018**, *553*, 63.
[25] K. Bogaert, S. Liu, J. Chesin, D. Titow, S. Gradecak, S. Garaj, *Nano Lett.* **2016**, *16*, 5129.
[26] I. H. Abidi, S. P. Giridhar, J. O. Tollerud, J. Limb, M. Waqar, A. Mazumder, E. L. Mayes, B. J. Murdoch, C. Xu, A. Bhoriya, *Adv. Funct. Mater.* **2024**, *34*, 2402402.
[27] W. Wu, Q. Zhang, X. Zhou, L. Li, J. Su, F. Wang, T. Zhai, *Nano Energy* **2018**, *51*, 45.
[28] K. Ye, L. Liu, Y. Liu, A. Nie, K. Zhai, J. Xiang, B. Wang, F. Wen, C. Mu, Z. Zhao, *Adv. Opt. Mater.* **2019**, *7*, 1900815.
[29] Y. Chen, M. Sun, *Nanoscale* **2021**, *13*, 5594.
[30] Y. Gong, J. Lin, X. Wang, G. Shi, S. Lei, Z. Lin, X. Zou, G. Ye, R. Vajtai, B. I. Yakobson, *Nat. Mater.* **2014**, *13*, 1135.
[31] W. Liu, J. Benson, C. Dawson, A. Strudwick, A. P. A. Raju, Y. Han, M. Li, P. Papakonstantinou, *Nanoscale* **2017**, *9*, 13515.
[32] P. Prajapat, P. Vashishtha, G. Gupta, *Small* **2025**, https://doi.org/10.1002/smll.202411596 .
[33] Y. Zhang, Y. Zhang, Q. Ji, J. Ju, H. Yuan, J. Shi, T. Gao, D. Ma, M. Liu, Y. Chen, *ACS Nano* **2013**, *7*, 8963.
[34] C. Lee, B. G. Jeong, S. H. Kim, D. H. Kim, S. J. Yun, W. Choi, S.-J. An, D. Lee, Y.-M. Kim, K. K. Kim, *npj 2D Mater. Appl.* **2022**, *6*, 67.
[35] C.-C. Huang, H. Wang, Y. Cao, E. Weatherby, F. Richheimer, S. Wood, S. Jiang, D. Wei, Y. Dong, X. Lu, *ACS Appl. Mater. Interfaces* **2022**, *14*, 42365.
[36] P. Vashishtha, I. H. Abidi, S. P. Giridhar, A. K. Verma, P. Prajapat, A. Bhoriya, B. J. Murdoch, J. O. Tollerud, C. Xu, J. A. Davis, *ACS Appl. Mater. Interfaces* **2024**, *16*, 31294.
[37] F. Wu, Q. Li, P. Wang, H. Xia, Z. Wang, Y. Wang, M. Luo, L. Chen, F. Chen, J. Miao, *Nat. Commun.* **2019**, *10*, 4663.
[38] P. Vashishtha, P. Prajapat, K. Kumar, M. Kumar, S. Walia, G. Gupta, *Surfaces Interfaces* **2023**, *42*, 103376.
[39] W. Yin, J. Yang, K. Zhao, A. Cui, J. Zhou, W. Tian, W. Li, Z. Hu, J. Chu, *ACS Appl. Mater. Interfaces* **2020**, *12*, 11797.
[40] L. Zeng, L. Tao, C. Tang, B. Zhou, H. Long, Y. Chai, S. P. Lau, Y. H. Tsang, *Sci. Rep.* **2016**, *6*, 20343.
[41] A. Verma, P. Chaudhary, R. K. Tripathi, B. F. Yadav, *Mater. Adv.* **2022**, *3*, 3994.
[42] J. Kublitski, A. Fischer, S. Xing, L. Baisinger, E. Bittrich, D. Spoltore, J. Benduhn, K. Vandewal, K. Leo, *Nat. Commun.* **2021**, *12*, 4259.
[43] A. Pant, Z. Mutlu, D. Wickramaratne, H. Cai, R. K. Lake, C. Ozkan, S. Tongay, *Nanoscale* **2016**, *8*, 3870.
[44] A. R. Rezk, S. Walia, R. Ramanathan, H. Nili, J. Z. Ou, V. Bansal, J. R. Friend, M. Bhaskaran, L. Y. Yeo, S. Sriram, *Adv. Opt. Mater.* **2015**, *3*, 888.
[45] P. Prajapat, P. Vashishtha, G. Gupta, *APL Energy* **2024**, *2*, 046103.
[46] S. Liu, Y. Chen, W. Gao, W. Li, X. Yang, Z. Li, Z. Xiao, Y. Liu, Y. Wang, *Adv. Mater.* **2023**, *35*, 2303544.
[47] H. M. Hill, A. F. Rigosi, K. T. Rim, G. W. Flynn, T. F. Heinz, *Nano Lett.* **2016**, *16*, 4831.
[48] X. Hong, J. Kim, S.-F. Shi, Y. Zhang, C. Jin, Y. Sun, S. Tongay, J. Wu, Y. Zhang, F. Wang, *Nat. Nanotechnol.* **2014**, *9*, 682.
[49] J. Zhang, L. Du, S. Feng, R.-W. Zhang, B. Cao, C. Zou, Y. Chen, M. Liao, B. Zhang, S. A. Yang, *Nat. Commun.* **2019**, *10*, 4226.
[50] F. B. Sousa, L. Lafeta, A. R. Cadore, P. K. Sahoo, L. M. Malard, *2D Mater.* **2021**, *8*, 035051.
[51] H. Park, G. S. Jung, K. M. Ibrahim, Y. Lu, K.-L. Tai, M. Coupin, J. H. Warner, *ACS Nano* **2022**, *16*, 10260.
[52] R. Rosati, I. Paradisanos, L. Huang, Z. Gan, A. George, K. Watanabe, T. Taniguchi, L. Lombez, P. Renucci, A. Turchanin, *Nat. Commun.* **2023**, *14*, 2438.
[53] E. Malic, R. Perea-Causin, R. Rosati, D. Erkensten, S. Brem, *Nat. Commun.* **2023**, *14*, 3430.
[54] Z. Zhang, X. Zou, V. H. Crespi, B. I. Yakobson, *ACS Nano* **2013**, *7*, 10475.